PNAS RESEARCH ARTICLE | BIOPHYSICS AND COMPUTATIONAL BIOLOGY
APPLIED BIOLOGICAL SCIENCES

Modular DNA origami–based electrochemical detection of DNA and proteins

Byoung-jin Jeon[a,1,2], Matteo M. Guareschi[a,1], Jaimie Marie Stewart[b], Emily Wu[c], Ashwin Gopinath[c], Netzahualcóyotl Arroyo-Currás[d], Philippe Dauphin-Ducharme[e], Kevin W. Plaxco[f], Philip S. Lukeman[g,2], and Paul W. K. Rothemund[a,2]

Affiliations are included on p. 11.

Edited by Joseph Puglisi, Stanford University School of Medicine, Stanford, CA; received December 10, 2023; accepted October 15, 2024

The diversity and heterogeneity of biomarkers has made the development of general methods for single-step quantification of analytes difficult. For individual biomarkers, electrochemical methods that detect a conformational change in an affinity binder upon analyte binding have shown promise. However, because the conformational change must operate within a nanometer-scale working distance, an entirely new sensor, with a unique conformational change, must be developed for each analyte. Here, we demonstrate a modular electrochemical biosensor, built from DNA origami, which is easily adapted to diverse molecules by merely replacing its analyte binding domains. Instead of relying on a unique nanometer-scale movement of a single redox reporter, all sensor variants rely on the same 100-nm scale conformational change, which brings dozens of reporters close enough to a gold electrode surface that a signal can be measured via square-wave voltammetry, a standard electrochemical technique. To validate our sensor's mechanism, we used single-stranded DNA as an analyte, and optimized the number of redox reporters and various linker lengths. Adaptation of the sensor to streptavidin and Platelet-Derived Growth Factor-BB (PDGF-BB) analytes was achieved by simply adding biotin or anti-PDGF aptamers to appropriate DNA linkers. Geometrically optimized streptavidin sensors exhibited signal gain and limit of detection markedly better than comparable reagentless electrochemical sensors. After use, the same sensors could be regenerated under mild conditions: Performance was largely maintained over four cycles of DNA strand displacement and rehybridization. By leveraging the modularity of DNA nanostructures, our work provides a straightforward route to the single-step quantification of arbitrary nucleic acids and proteins.

DNA origami | biosensor | square-wave voltammetry | modular sensor | electrochemistry

Significance

Aptamer-based, conformation-switching electrochemical biosensors enable real-time analyte sensing in the living body. However, developing sensors for new analytes is limited by the difficulty of optimizing electrochemical signal strength and gain, without compromising binding properties of the aptamer. Optimization of new sensors often requires synthesis of many expensive, multiply modified oligonucleotides. In contrast, we describe a reagentless DNA origami-based platform whose binding and signaling properties are essentially independent. This independence enables signal optimization to be based on analyte size; sensors are customized using a library of inexpensive and unmodified DNA linkers. This library is portable between different sensor designs and analytes. Our work thus provides a "toolkit" for constructing electrochemical biosensors, and a general approach for modular biosensors beyond electrochemical detection.

DNA nanotechnology (1, 2) enables the design and construction of artificial structures with nanometer precision via sequence-specific assembly of DNA oligonucleotides. Such structures (e.g., branched DNAs and tetrahedra, 3–6) are often used as scaffolds for biosensors, wherein DNA-coupled binding components, such as aptamers, antibodies, or small-molecule ligands produce a signal upon introduction of a cognate analyte molecule. DNA origami (7, 8), provides an architecture for making 100-nanometer scale structures of arbitrary geometry, with hundreds of attachment sites for active components such as binders or reporters. Thus, DNA origami is of particular interest for biosensors (9–11) because it allows the synthesis of reconfigurable structures that undergo large conformational changes (tens or hundreds of nanometers, 12–27), rearranging large numbers of reporters (tens or hundreds, 23) that amplify molecular binding events to the point that they can be reliably detected.

Reconfigurable origami sensor platforms can be divided into broad classes based on their readout mechanism, with each mechanism having advantages and disadvantages. Atomic force microscope (AFM)-based platforms, for example, such as "DNA forceps" (12, 13) or "picture frames" (14) enable the direct visualization of single molecule reconfiguration as a function of protein binding (12), pH (13), or ionic conditions (14) but they require expensive AFMs and time-consuming measurements. Single-molecule fluorescence, optical tweezers, and magnetic tweezers-based platforms (15–18) exhibit extraordinary temporal resolution for the reconfigurations of single molecules, and enable the dissection of sensor states that could otherwise not be resolved. But, as for AFM, the required equipment is expensive and the measurements time-consuming. Gel electrophoresis-based platforms (19) for protein or nucleic acid detection are relatively inexpensive and can be multiplexed (20). However, these measurements are slow, at best taking tens of minutes. Fluorescence resonance energy transfer (FRET) platforms have provided simple bulk measurements of DNA (21) and protein (22) down to the

Competing interest statement: A patent related to this work with inventors A.G. and P.W.K.R. was issued as U.S. patent 11,391,734 to California Institute of Technology and licensed to Somalogic, Inc.

This article is a PNAS Direct Submission.

[1]B.J. and M.M.G. contributed equally to this work.

[2]To whom correspondence may be addressed. Email: bjeon83@gmail.com, lukemanp@stjohns.edu, or pwkr@dna.caltech.edu.

This article contains supporting information online at https://www.pnas.org/lookup/suppl/doi:10.1073/pnas.2311279121/-/DCSupplemental.

Published December 30, 2024.

100 nM range; achieving 100 pM has required expensive single-molecule FRET microscopy (23). Chiral plasmonic platforms have enabled simple bulk sensing of nucleic acids (24, 25) and small molecules (26, 27) achieving 100 pM sensitivity for RNA, but spectrometers capable of measuring circular dichroism are relatively expensive. Layered on top of these concerns, few of these approaches have been shown to work in complex biological sample matrices, and none of the above platforms appear easily extendable to in vivo measurements.

In contrast to these techniques, an electrochemical platform based on the conformation-switching of single-stranded DNAs (28) enables real-time measurements of analytes using inexpensive potentiostats (29). By using miniaturized electrode implants, analytes can be quantified in challenging environments such as living animals (30, 31). This platform uses a gold electrode, protected with an alkanethiol monolayer— the electrode is further functionalized with a target-binding oligonucleotide that displays a gold-binding thiol on one end of the oligonucleotide, and a redox-reporter (most commonly methylene blue, "MB") distal to the thiol. Upon interacting with its target, for example during DNA hybridization ("E-DNA sensors," 32–34) or aptamer–molecule binding ("E-AB sensors," 35–37), the oligonucleotide undergoes changes that affect the rate of electron transfer between the reporter and the electrode surface. When the electrode is brought to the reduction/oxidation potential of the reporter, current is thus measured as a function of binding state of the oligonucleotide.

In the most common model of E-AB sensor operation, analyte binding-induced reconfiguration of the aptamer structure changes the collision frequency of the redox reporter with the electrode surface, changing the electron transfer rate and thus measured current (38). Analyte binding in E-AB sensors is transduced into a signal by a unique and idiosyncratic binding-induced nanometer-scale movement; this conformational change *differs between different aptamers* (e.g., see differences between thrombin and IgE aptamers in ref. 38) and it is evident that binding and signal transduction depend on each other in complex ways. Thus, making sensors for new analytes with both good signal gain (relative change in signal upon target saturation) and appropriate affinity and selectivity often requires optimization, with multiple rounds of semiempirical redesign and resynthesis of expensive modified oligonucleotides (39). Spectroscopy-guided approaches to aptamer probe redesign (40) shorten but do not eliminate this onerous process. Special "capture SELEX" techniques that select for conformational change of the aptamer (41, 42) rather than simple binding, can increase the likelihood of obtaining suitable switching aptamers but cannot guarantee success.

The question arises: Might the advantages of reconfigurable DNA origami and E-DNA/E-AB systems be combined? Several recent publications explore DNA origami in the context of electrochemical sensing. For example, the capacity of origami to display multiple binders has been used for an electrode-bound miRNA sensor, wherein origami acts as a substrate that presents multiple miRNA binding sites (43). Likewise, a pH sensor has been reported that employs a reconfigurable DNA origami "zipper" bound to a gold electrode (44), and electrode-bound origami were used to probe the spatial dependence of redox-active enzyme activity (45). Free DNA origami rectangles have been used to amplify signal from DNA analytes (46); the detection of free origami rectangles themselves represents an elegant demonstration of nanoimpact electrochemistry (47). Unlike E-AB/E-DNA systems, however, these origami-based systems are not reagentless; they all require the addition of redox mediators to the analyte solution to generate electrochemical signals, which limits their use in vivo or in other environments where these mediators are not available. And aside from the pH-responsive zipper (44), none of the above systems use large-scale conformational reconfigurations for signal transduction.

One reconfigurable origami-based electrochemical sensor that uses MB reporters instead of added redox mediators, has been reported (48). Intended to detect 100 nm scale analytes such as viruses, this system requires significant modification for analytes of different sizes. Furthermore, as configured, it is a "signal-off" device, for which analyte binding results in a lower current; this limits both the signal gain (at best, −100%; see formula for gain below) and confidence that signal change is not caused by sensor degradation.

In this work, we introduce a reconfigurable DNA origami sensor whose modular architecture overcomes the redesign and optimization challenges posed by E-DNA and E-AB sensors. By combining a flat, two-dimensional DNA origami with a double-stranded DNA (dsDNA) linker, we create a "lily pad" structure wherein origami, decorated with numerous MB redox reporters are tethered to an ultraflat gold electrode via a long and flexible dsDNA linker (Fig. 1). This open conformation is converted to a closed conformation by the presence of analyte biomolecules when they bind and form a bridge between a pair of probes on the origami and on the electrode surface. The resulting conformational change is detected via square-wave voltammetry (SWV, Fig. 1 *B*, *Inset*), in which the current, which is a function of the rate of electron transfer between MB molecules and the electrode surface, increases with proximity.

The lily pad architecture described above is reminiscent of a classical sandwich assay, in which a pair of affinity binders is used to localize a signaling system to a surface if and only if the target analyte attaches to both binders: The first binder, or "capture" reagent, is attached to a surface; addition of sample results in target analytes being bound to capture reagents via a first epitope; further addition of a labeled "detect" reagent that binds the analyte at a second orthogonal epitope provides a mechanism to generate signal. Simple binders, rather than the structure-switching binders of E-AB systems, are all that is required; industry has generated many thousands of capture-detect antibody pairs for commercial assays. Indeed, antibody pairs have been incorporated into a number of electrochemical assays—yet these systems are not reagentless, typically requiring both 1) a step involving physical addition of the detect reagent and 2) incorporation of an amplification system (typically attached to the detect reagent) such as an enzyme (50), or hybridization chain reaction (51).

Given their success elsewhere in biosensing, it is interesting to ask why pairs of sandwich antibodies have not proven amenable to reagentless electrochemical sensing. Reagentless sensors require 1) that all of their components, from the binders to any detection system to be built into a single, intramolecular device, which reconfigures upon analyte binding and 2) that the reconfiguration be able to work with the detection system to create a signal of sufficient magnitude. The first requirement might in principle be solved by a simple linker between the binders, but the second requirement turns out to be a more fundamental problem. In typical sandwich immunoassays, the stack formed by the capture reagent, analyte, and detect reagent is at least several nanometers in height, e.g., 10 nm in the case of bovine serum albumin with two antibodies (52). To render the device reagentless, some component has to be directly labeled with a redox reporter; labeling either antibody would result in a geometry for which electron transfer to the surface is too slow for sensitive detection [for E-AB sensors, electron transfer rates drop off significantly a few nm from the electrode surface (53)]. Using smaller binders in sandwich assays, e.g., nanobodies (54), could help increase the range of

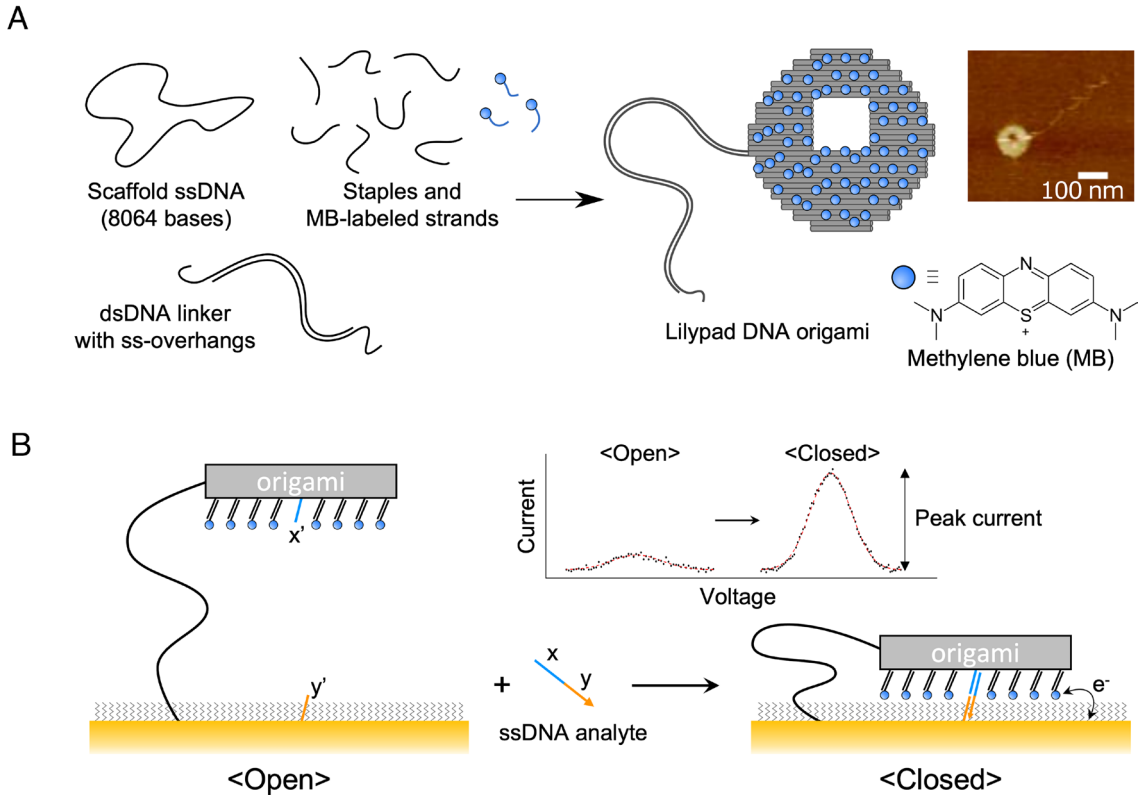

Fig. 1. Lily pad sensors can be used for the electrochemical detection of biological analytes, here a DNA single strand. (*A*) A flat, disk-shaped DNA origami with a square hole (49) carrying a long dsDNA linker is assembled from a mixture of long ssDNA scaffolds, ssDNA staples, 70 staples with 5′ extensions for MB reporters and for analyte binding, 20 nt MB-modified DNA oligos, and long dsDNA linkers with ssDNA overhangs at both ends. *Inset* shows AFM of a lily pad. (*B*) Two types of thiol-modified ssDNA are immobilized on a template-stripped gold surface: one for tethering the lily pad origami via hybridization with one of the linker overhang sequences, and the other for analyte binding to the gold surface. Closing events occur when a DNA analyte binds both to the binding site on the origami and the binding site on the surface, enabling electron transfer between MB reporters and the gold electrode. *Inset* shows an exemplary square-wave voltammogram of a sensor in the open state (*Left*), and a voltammogram in the closed state after DNA analyte addition (*Right*). The peak current is calculated as the heights of the peaks relative to the underlying baseline.

accessible analytes, but the use of smaller binders in this context merely shifts the limiting factor to analyte size. This length scale problem has limited development of reagentless electrochemical sandwich immunoassays. A cleverly designed system (55) utilizes a combination of DNA linkers with an antibody pair, in a geometry that positions a MB reporter at the very base of the sensor in the analyte-bound state. This results in an antibody sandwich acting as a highly sensitive, amplification-free, electrochemical sensor whose performance does not depend strongly on the size of the binders or analyte. However, that sensor still requires addition of DNA-labeled antibodies in solution and thus does not operate in a reagentless mode.

Here, our lily pad design overcomes the problem of large binder–analyte sandwiches through its use of numerous MB reporters which project down from the origami in a flexible "curtain" around the sandwich that extends at least 5 nm toward the surface. Like E-DNA/E-AB systems, our lily pad incorporates all components in a single, intramolecular construct rendering it reagentless. Unlike the E-DNA/E-AB systems the lily pad is more easily adapted to other analytes—by simply exchanging unmodified strands for linkers and curtain length we demonstrate the detection of DNA and two different proteins.

Results

Lily Pad DNA Origami Device. Fig. 1 shows the design of our lily pad device. The device consists of a 100 nm diameter disk-shaped DNA single-layer origami designed on a square lattice, starting from a previously published model (49). During folding (*Materials and Methods*), the origami is attached to a long dsDNA linker (Fig. 1*A*) which, depending on experiment, ranges from 300 to 3,000 base pairs (bp) in length. The distal end of the linker is attached to a gold electrode through DNA hybridization: The distal end of the linker displays a single-stranded DNA (ssDNA) overhang, and binds to a complementary ssDNA that is immobilized on the gold electrode. E-DNA/E-AB sensors often use roughened gold electrodes to maximize the surface area for their small ssDNA sensing molecules (56, 57), despite the resultant structural heterogeneity of such electrodes. Here, in contrast, we use ultraflat, template-stripped gold chips (58) to minimize the distance between the entire bottom face of the origami disk and the electrode surface upon analyte binding. Our lily pad sensors use 70 MB molecules as reporters to transfer electrons to the electrode; they are attached to one side of each origami via 20 bp-long ssDNAs hybridized to overhangs on 70 modified staple strands (Fig. 1*B*)—this forms a curtain of MB-modified DNA strands hanging from the origami. Detection of a ssDNA analyte sequence *xy* is achieved through binding to two DNA sequences, x' and y', which are complementary to subsequences x and y of xy, respectively. Sequence x' is positioned on the origami as an extension to a central staple, and a thiol-modified version of y' is immobilized on the gold electrode surface via an Au-S bond. When both x and y in a DNA analyte bind to x' and y' on the lily pad and the underlying electrode, the conformation of the lily pad changes from the "open" to the "closed" state. Each closing event brings the 70 MB curtain into proximity with the gold surface, facilitating electron transfer between MB and electrode and increasing voltammetric peak currents (Fig. 1 *B*, *Inset*).

The distance between MB molecules and the electrodes, which determines the electron transfer rate, is set by the particular probe–analyte binding geometry (59). We note that in the open, unbound state, the relative average position of the MB redox reporters with respect to the surface is a function of the flexibilities of the dsDNA linker, origami (60, 61), and MB attachment; therefore, we would expect background signal even in the absence of analyte (see below). Background signal is observed with E-DNA and E-AB sensors for similar reasons (33, 62), and it is observed here (Fig. 1 *B*, *Left* side of *Inset*).

For the closed, bound state, the same factors should affect electron transfer rate, with the exception that the distance between the lily-pad's reporters and the surface should be independent of the dsDNA linker length. We estimate the reporter–surface distance for the closed state by noting that the length of the bound DNA analyte is 28 bp (~9.8 nm); as the tail length is 20 bp (~6.8 nm) for the reporter strands, this difference leaves the redox reporters nominally ~3.0 nm away from the surface on average (Fig. 2 *A*, blue *Inset*). Were the MB rigidly held at this position, thirty times the electron transfer decay distance (63), electron transfer rates would be unmeasurably slow; thus we suspect that bending fluctuations of the origami cause MB to visit distances less than 3 nm from the surface, enabling electron transfer from the MB curtain to be observed.

In principle, more MB units per lily pad should generate a greater signal upon analyte binding. However, saturation MB modification (1 MB per staple) leads to aggregation of origami during annealing, potentially due to the DNA intercalation of MB, electrostatic DNA backbone–MB interactions, or concentration-dependent dimerization of MB (64, 65). Optimizing lily pad MB density while minimizing aggregation, we found that the use of 70 MB-modified extensions results in lily pads that run as monomers in agarose gels, while higher numbers of MB reporters lead to poorly formed structures that aggregate and remain stuck in gel wells (for optimization see *SI Appendix*, Fig. S1 and Table S1).

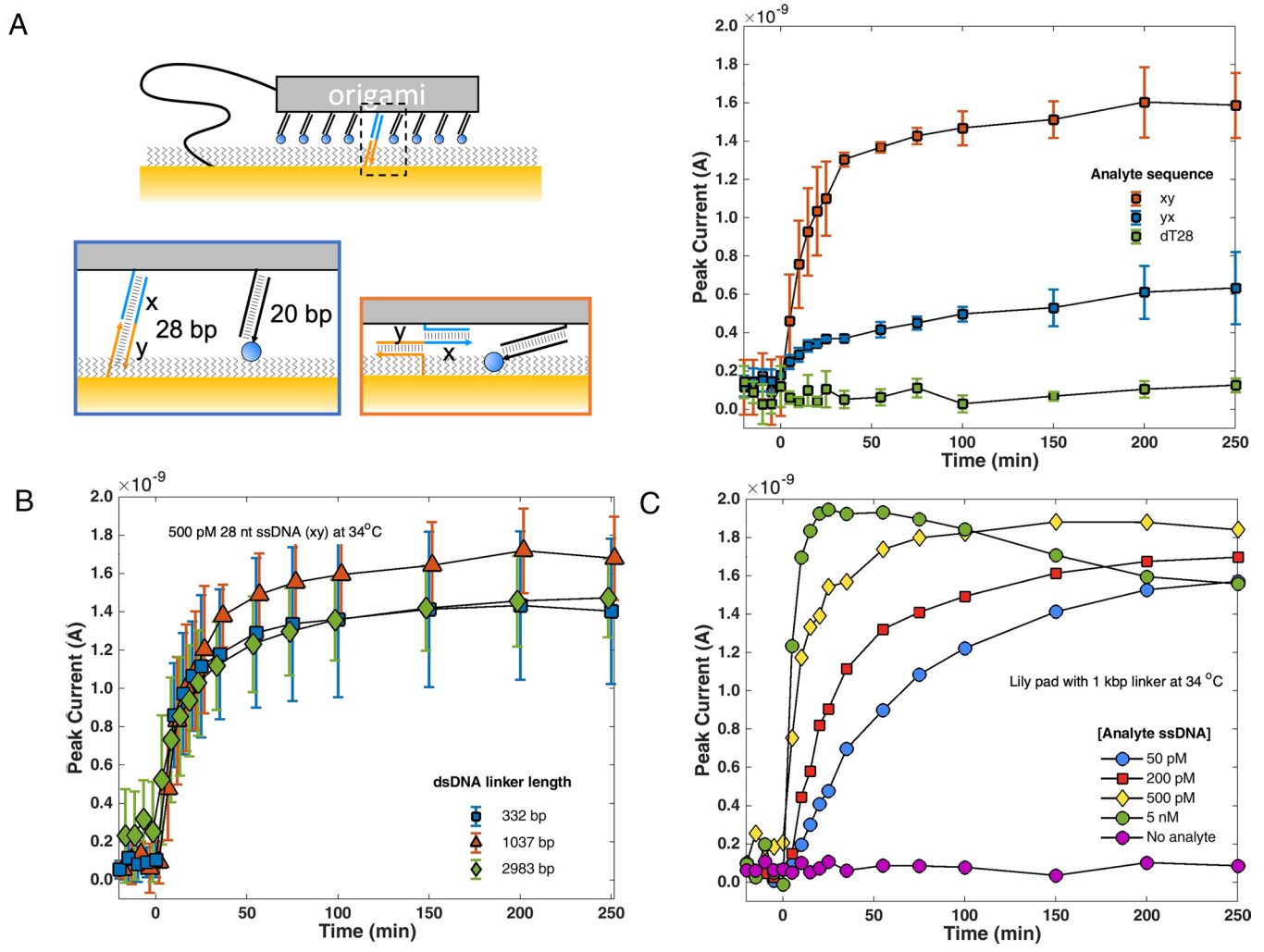

Fig. 2. Lily pad closing events can be monitored via voltammetry in real-time. (*A*) 500 pM of each of three different ssDNA analytes, with 28-bp sequences *xy* (blue), *yx* (orange), and *dT* (green) were added at time *t* = 0 at 34 °C. The difference in kinetics for *xy* and *yx* binding can be understood in terms of difference in spacing between the origami and gold surface in their respective bound states (*Bottom Left*). For *yx* to bind (orange box), the origami must get much closer to the surface than in the case of *xy* (blue box), incurring an increased entropy penalty. Binding of *yx* may also be sterically hindered by the 20 bp long MB reporters that comprise a curtain projecting down from the origami (*Top Left*). The *dT28* analyte is a noncomplementary sequence and is not expected to trigger any binding event. Experiments were performed on three different chips and are shown as a line for the average and error bars for the SD. (*B*) The length of the linker tethering the lily pad to the surface has little effect on sensor response: linker lengths of 332, 1,037, and 2,983 bp all show comparable behavior. Experiments were performed on three different chips and are shown as a line for the average and error bars for the SD. So that overlapping error bars from different experiments can be compared, jitter was added to the *x*-axis. (*C*) The functional form of sensor response varies with the concentration of ssDNA analyte. At analyte concentrations up to 500 picomolar (yellow diamonds), sensor response increases monotonically. At nanomolar concentrations (green circles), the system shows saturation effects, and the current decreases after 1 h, potentially due to excess free analyte in solution reopening previously closed lily pads via DNA strand displacement. ssDNA analyte *xy* added at *t* = 0.

Chip Preparation and Electrochemical Measurement. Ultraflat gold chips were fabricated via template-stripping (58, 66). This approach had the added benefit of revealing an extremely clean surface upon removal of the template. Two different thiol-modified ssDNA were immobilized on gold surfaces, one that binds the DNA origami linker and one that binds the analyte molecule. The surface was then backfilled with a passivation layer of 6-mercapto-1-hexanol in order to minimize a spurious current from oxygen reduction (67). The chip was incubated with lily pad DNA origami structures and then used as the working electrode in a three-electrode cell.

DNA Detection. In the absence of analyte, SWV of the lily pad functionalized chip resulted in a baseline voltammogram (an example of which is shown in Fig. 1 *B*, *Inset*; "Open" state) with a peak current at ~−0.27 V, which coincides with the reduction potential of methylene blue (35, 68). We note that the baseline was not observed before incubation of the electrode in the lily pad solution. The stiffness of dsDNA, as measured by its persistence length of ~150 bp (69, 70), is too short for the 1 kbp dsDNA linker to rigidly hold the lily pads away from the surface. Thus, baseline signal, which typically ranges from 0.05 to 0.3 nA, is likely partially due to thermal fluctuations that bring the MB-modified origami close to the surface. When MB-origami without dsDNA linker are added and rinsed away, we have observed a baseline as high as 0.06 nA. Thus, part of the baseline signal may also be attributable to nonspecific binding of the MB-origami part of the lily pad, or free MB labeled strands. Baselines in the 0.05 nA range are at the limit of our methods to extract meaningful currents, and thus other methods will be necessary to dissect the contributions of tethered yet fluctuating lily pads versus nonspecifically bound MB-origami or MB-labeled strands.

Similar baselines were observed for all the SWV presented in this work, and were observed to be stable for over 6 h and up to four sensor regenerations (i.e. in the penultimate figure of this paper). In general, the baseline provides a reference state from which the occurrence of binding events can be inferred.

Upon challenging the sensor with the fully complementary ssDNA analyte *xy*, an increase in SWV signal from baseline was observed (Fig. 1 *B*, *Inset*), resulting in sensorgrams (Fig. 2*A*, blue curve) similar to those resulting from other real-time surface-bound, DNA hybridization biosensors that use surface plasmon resonance (SPR), biolayer interferometry (BLI), and the E-DNA platform (33, 48, 71–73). In addition, this sensorgram demonstrates that, at 500 pM analyte DNA concentration, we observe an increase in current from 0.124 nA to a plateau of 1.58 ± 0.17 nA (i.e., $\left[\frac{I_{peak\ for\ saturation}}{I_{peak\ for\ blank}}\right] \times 100 \approx 1,270\%$ gain after 250 min of target incubation. For reference, benchmark *optimized* E-DNA ssDNA-detecting sensors displayed gains of 260% (74); optimized E-AB sensors have reached 430% (75). Encouraged by these unprecedented gains, we proceeded to test the effects on sensor response of varying the lily pad and analyte structure.

For DNA analytes oriented perpendicularly to the surface, like *xy* (Fig. 2 *A*, blue *Inset*), we expected that longer analytes (up to duplex DNA's persistence length) could decrease signal gain by preventing close approach of the 20 bp MB curtain. By switching the positions of the *x* and *y* to yield a sequence (*yx*), the orientation of the analyte was changed to be parallel to the surface (Fig. 2 *A*, orange *Inset*), without significantly affecting predicted thermodynamics. We originally hypothesized that using this orientation could make signal gain independent of length. However, we observed (Fig. 2 *A*, *Right*) slower on-signal kinetics (the rate of signal increase upon addition of analyte) and lower signal at the end of the experiment compared to the *xy* analyte, presumably due to the length of the MB curtain which appears to be a significant steric obstacle for the origami to successfully close. For practical reasons, we did not pursue this approach further, but note that shorter MB curtains might recover signal gain and achieve the goal of DNA length-independent signal.

To explore the effect of the lily pad linker length on sensor performance, we synthesized and tested double-stranded DNA linkers of three different lengths: 332, 1,037, and 2,983 bp (Fig. 2*B*). We challenged these lily pads with 500 pM of *xy* ssDNA analyte; the average behavior of all three sensor types was similar (Fig. 2*B*; blue, red, and yellow data) in terms of baseline signal (0.17 ± 0.07 nA), initial on-signal kinetics (~0.09 nA/min up to 10 min), and endpoint signal (1.49 ± 0.08 nA). Given these results, we arbitrarily chose to use the 1,037 bp linker for all subsequent experiments.

Fig. 2*C* shows the sensor response to increasing concentrations of DNA analyte. For times less than an hour, both signal and signal kinetics (the rate of signal growth) increase monotonically with concentration. After an hour, two behaviors are observed: 1) signal for analyte concentrations less than 5 nM continues to increase, and 2) signal for an analyte concentration of 5 nM undergoes a surprising decrease. This bifurcation in behavior is reminiscent of the "high dose hook effect" (76) which occurs when excess analyte saturates both binders of a sandwich sensor, preventing sandwich formation and decreasing signal. Because the present hook effect emerges over the course of a time-based sensorgram, we term it the "kinetic hook effect" (see *SI Appendix*, section 6 for discussion).

Optimizing a Multimeric Protein Detector. Because of the lily pad's modularity, it is trivial to modify into a detector for multimeric proteins with multiple identical binding sites. As a proof-of-principle (Fig. 3), we prepared lily pad sensors for detection of a model multimeric protein, streptavidin. We achieved this by simply adding two biotinylated adaptor strands to our basic DNA-sensing chips (Fig. 3*A*): The first adaptor, sequence *x*, was complementary to the 14 nt ssDNA tail (*x*′) on the origami; the second, sequence *y*, was complementary to the 14 nt oligos (*y*′) on the surface. Thus, chips with the lily pads used for ssDNA detection were incubated with the biotin-modified adaptors to obtain streptavidin detectors. To optimize sensor design, we measured sensor response as a function of both surface linker length (L = 14, 24, 34 or 44 bp) and MB curtain length (l_{MB} = 20, 40, or 60 bp).

Because it is measured before streptavidin addition when the lily pad is nominally open, the baseline was expected to be independent of curtain length. However, the baseline (Fig. 3*C*) was almost always higher for l_{MB} = 40 and 60 bp than for 20 bp (only for L = 44 was the 40 bp baseline slightly smaller than the 20 bp baseline). Part of the baseline is thus apparently due to transient sticking of the curtain to the surface. To account for longer curtain's enhanced stickiness, we suggest that either 1) longer curtains access MB configurations which are individually stickier, e.g., with more MB contacting the surface or 2) longer curtains have an increased total number of weakly sticky MB configurations.

When streptavidin was added to l_{MB} = 20 bp sensors, the SWV signal quickly increased, reaching ~50% or more of the final signal change within 5 min after streptavidin addition. For each $L \leq 34$, comparatively slower on-signal kinetics were observed for l_{MB} = 40 bp and 60 bp sensors. The slower kinetics observed for 40 and 60 bp MB curtains (most noticeably for L = 14) was similar to

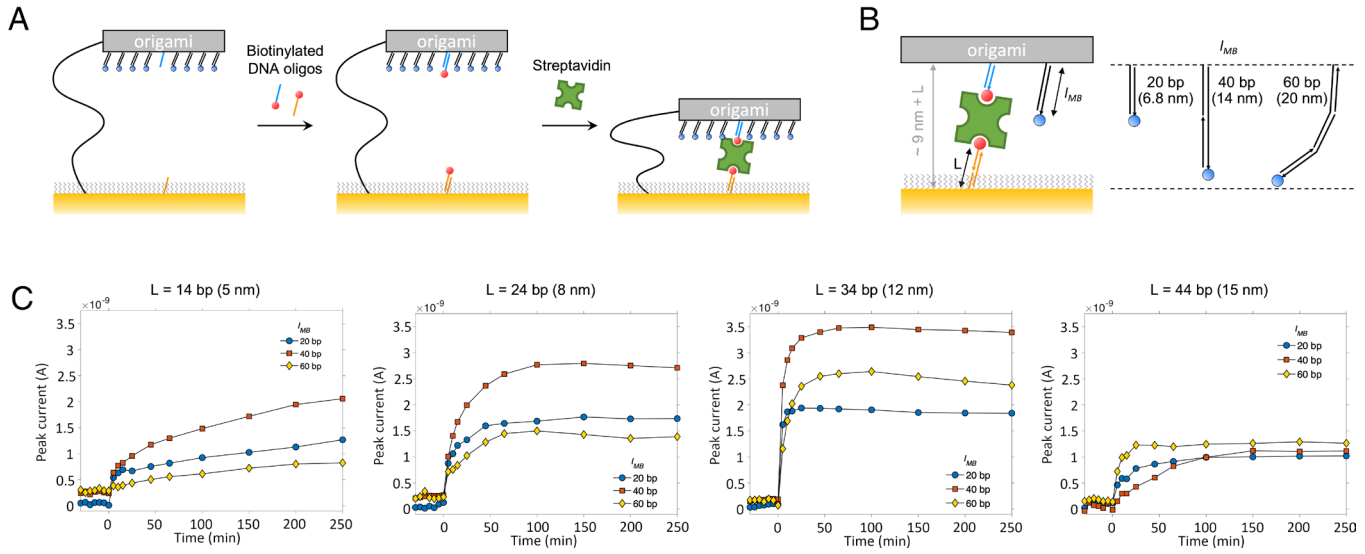

Fig. 3. Lily pad sensors for DNA can be readily converted into protein sensors and their response rationally optimized. (*A*) Two biotinylated ssDNA adaptors are hybridized to the sequences *x* and *y* on the origami and on the surface to create a streptavidin sensor. (*B*) Different lengths for the MB-modified DNA curtain, l_{MB}, and dsDNA linkers for the surface biotin, *L*, were created to study the effect of molecular design on sensor behavior. (*C*) SWV sensorgrams for streptavidin (500 pM) detection with various MB curtain lengths (20, 40, and 60 bp) on origami and dsDNA linker lengths (14, 24, 34, and 44 bp) on the surface. Different l_{MB} and *L* give qualitatively different results for both on-signal kinetics and endpoint signal. Longer MB curtains increasingly disturb the closing of the lily pads, but at the same time bring MB closer to the gold surface, increasing peak current; the origami shape itself may have a steric clash with the surface that changes with the length of the analyte–binder complex. The maximum in peak current (40 bp for L = 14, 24, 34, and 60 bp for L = 44) as a function of curtain length is likely set by the tensions between these three effects. Overall, a 40 bp MB curtain and 34 bp surface linker yields the largest signal change.

that observed for detection of the 28 nt DNA reversed sequence, *yx* (Fig. 2*A*), and we interpret it similarly, i.e., we believe that the longer MB curtains sterically hinder sensor closing. However, at L = 44, the analyte–binder complex has moved curtains of all lengths sufficiently far from the surface that steric effects are minimal; l_{MB}= 60 bp curtains, extending closest to the surface, gave the fastest kinetics.

We expected to see the largest effect of sensor design in peak current endpoints; some experiments showed small decreases in peak current after extended interrogation and so we compared maximum peak currents (MPC) over the 250 min experimental window. Our goal was to optimize signal change and our hypothesis was that trends in sensor performance should be interpretable in terms of the difference δL between the total size of the binder–analyte complex and the MB curtains. In an optimal sensor design, the closed lily pad conformation should bring the redox reporters as close as possible to the surface without a steric clash. Absent any tilting of the curtain strands, one might expect to see steric clashes for $\delta L < 0$. In our DNA sensor above, a 28 bp analyte–binder complex (9.5 nm) was used with a 20 bp MB curtain (6.8 nm) that was slightly shorter (by δL = 2.7 nm); in this configuration (Fig. 2) the DNA sensor achieved an MPC of 2.75 nA. *SI Appendix*, Table S6 gives δL and MPCs for all conditions in Fig. 3*C*. For three of the four conditions (cyan and yellow; *SI Appendix*, Table S6*A*) with δL most similar to the DNA sensor (<1.8 nm different), MPCs were ≥75% that of the DNA sensor. But a fourth condition was only 45%. Further, four pairs of conditions having the same δL (but different L and l_{MB}) had markedly different MPC. This analysis shows that δL alone is not a good predictor of MPC.

Instead, observe that for *all three curtain lengths* (and thus a wide range of δL), MPC has a maximum for L = 34 before steeply dropping off for L = 44. At this boundary, the ranking of which MB curtain length gives the highest MPC also abruptly changes. Taken together, these observations suggest that there is some other steric effect, which changes sharply between L = 34 and L = 44, and which couples to the steric effect of the MB curtain length. Otherwise, we would expect a stronger correlation between MPC and δL across the boundary. In particular, we would expect an increase for the MPC of 60 bp curtains as L changes from 34 to 44, where δL goes from 0.92 nm to 4.3 nm. Rather we see a drop in MPC from 2.6 nA to 1.25 nA—for comparison, a large δL of 14.5 nm still achieves an MPC of 1.9 nA for 20 bp MB curtains at L = 34.

We propose that the origami shapes exhibit either large deformations (either static or dynamic) from a flat disk, on the order of ~21 nm in height (the size of the analyte–binder complex for L = 34). One possible source of deformation is that the MB curtain causes the origami to curl into a U-shaped cross-section that bends up and away from the surface: Simulations of origami with MB curtain-like extensions predict such deformations at the 20 nm scale (77); similar-sized fluctuations of 2D origami have been observed experimentally (78). Perhaps for L = 34 and below, these deformations allow MB curtains of any length to contact the surface, and so increasing L up to 34 decreases steric interference between the MB curtain and the surface. By L = 44 (corresponding to an analyte–binder complex of 25 nm), all curtain lengths are held too far from the surface for deformations of the origami to bring them into contact. The longest curtains (60 bp, ~20 nm) give the highest MPC at L = 44, as they position MB closest to the surface in this "noncontact" regime.

While the dependence of sensor performance on the size of the analyte–binder complex and the MB curtain length is not as simple as we first envisioned, it is nevertheless intelligible. The library of linker and curtain strands we have developed are analyte agnostic. Thus, our experiments provide a procedure and map for how sensors for other analytes can be optimized.

Having determined that the optimal (highest MPC) lily pad design for streptavidin detection has a 40 bp MB curtain and L = 34 bp linker, we sought to assess the linearity of this sensor and measure its sensitivity (LoD). We thus challenged this design with concentrations of streptavidin, ranging from 1 pM to 1 nM (Fig. 4). Signal change was plotted as a function of the streptavidin concentration in Fig. 4 on a semilog scale. The signal increased

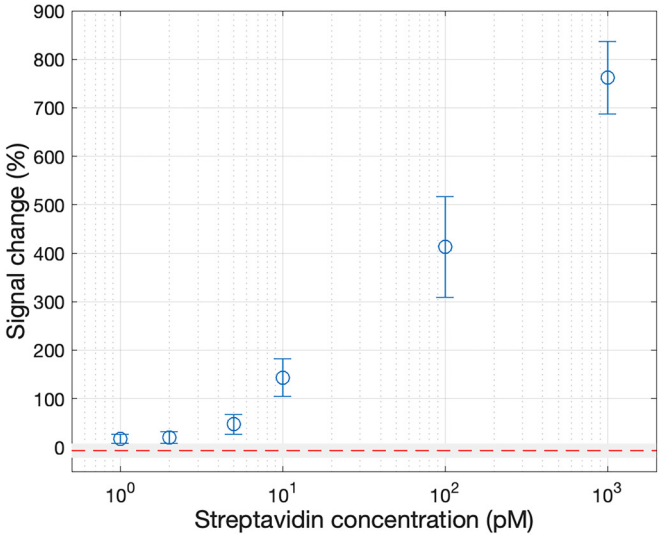

Fig. 4. Lily pad sensors can quantify picomolar protein concentrations. SWV signal changes were measured for lily pads having 40 bp MB curtains and L = 34 bp linkers using six streptavidin concentrations from 1 to 1,000 pM and a blank (zero analyte). Mean and SD for each concentration were calculated from replication using five different chips (five biological replicates). On each chip, the off-signal (before sample application) was measured five times and averaged (five technical replicates). After sample application and incubation (1 h, 34 °C) the on-signal (endpoint signal) was measured five times and averaged (five technical replicates). Signal changes in the interval $\mu_0 \pm 3\sigma_0$ are shaded gray, where μ_0 is the mean of the blank and σ_0 its SD. LoD < 1 pM.

monotonically from 2 pM up to 1 nM, with log–linear behavior observed between 5 pM and 1 nM. Using these data, we estimated the limit of detection (LoD) by the conventional method (79, 80), wherein $\mu_0 + 3\sigma_0$ is the signal at the LoD concentration, σ_0 is the SD of the blank ([streptavidin] = 0) and μ_0 is the mean of the blank. Here, $\mu_0 + 3\sigma_0$ = 8.0%, where μ_0 = −7.0% is sensor baseline in the absence of streptavidin (Fig. 4, red dotted line). Because [streptavidin] = 1 pM gives a signal change (17%) that is significantly larger than 8.0%, we infer that LoD < 1 pM.

As observed with the sensor for the ssDNA analyte *xy*, the gains reported for our optimized streptavidin sensor are unprecedented for a reagentless, unamplified, single-step electrochemical sensor. When challenged with 500 pM streptavidin in bulk solution (Fig. 3*C*), at steady state measurements past 50 min, gains for the 40 bp MB curtain and L = 34 bp linker system were greater than 1,600%. For experiments where the linearity of the sensor and LoD was determined (Fig. 4), gains at the same streptavidin concentration were calculated to be greater than 500%. We believe this difference is a function of the experimental conditions. For the steady state measurement, the electrochemical cell was left undisturbed with a large volume of bulk analyte solution (1 mL) and repeatedly interrogated over time. For the linearity/LoD measurement we 1) sought to model a situation with smaller, more practical sample volumes and thus used 10 µL rather than 1 mL, 2) sought to recycle chips and thus made multiple repeated measurements on the same chip, 3) sought to model an assay in which spuriously bound sample molecules are washed from the sensor before measurement, and thus the chip was washed with buffer before each baseline and each streptavidin measurement.

The remarkable size of our sensor's gains becomes clear through comparison with previously published systems. In comparison to our system, interrogation of other electrochemical streptavidin sensor platforms in buffered solutions gave maximal gains that were *at least an order of magnitude smaller* than our maximal lily pad gains. Furthermore, these other platforms' maximal gains were typically reached at significantly higher analyte concentrations. For example, a duplex E-DNA-like sensor displaying biotin gave maximal (in terms of magnitude) gains from −50% (signal-off) to +50% (signal-on) at 3 nM streptavidin (81). A modified version of this platform that relies on surface-based steric hindrance, gave −60% at 100 nM streptavidin (82). A DNA junction-based sensor gave −50% at 500 nM (83), and a modular, bivalent Y-shaped structure gave −43% at 100 nM (84). In addition, our sensor's LoD, <1 pM, represents an improvement of *at least two orders of magnitude* over the LoD of the streptavidin sensors described above. Given these dramatic gain and LoD improvements over existing sensor designs, we believe that the lily pad architecture offers a generalizable platform for high-sensitivity, high-gain measurements of analyte concentration.

Lily Pad Sensor Regeneration. The biotinylated DNA adapter strands were redesigned to have an additional 5 nt ssDNA toehold (Fig. 5*A* and *SI Appendix*, Table S3). This enables their removal via toehold-mediated strand displacement (85): A solution containing two 19 nt invading strands (*SI Appendix*, Table S3) whose sequences are fully complementary to the extended adapter strands is applied to the surface; subsequent strand displacement reexposes the 14 nt DNA-sensing tail (x) on the origami and the DNA sensing thiolated ssDNA (y) on the surface. Using a 100 nM concentration of applied invading strands, the analyte is displaced in 10 min; addition of 500 pM biotinylated adapter strands regenerates the sensor for further interrogation (Fig. 5*B*). We conducted four rounds of sensing, displacement, and regeneration in this manner, and the sensor responded to streptavidin with similar kinetics after each cycle.

However, it was observed that this process does not completely restore the sensor to its original state; up to ~5% loss in on-signal was seen after each round of regeneration (Fig. 5*C*). To explain this loss, we suggest that either 1) incomplete strand displacement leaves some streptavidin–biotin complex bound either to the origami or on the surface, blocking analyte binding sites in subsequent sensing rounds or 2) thiolated y may desorb from the surface. A third alternative is that 3) MB-strands or even entire lily pads are released with each regeneration; however, this is inconsistent with our observation that the raw baseline sensor signal did not decrease through rounds of regeneration. To achieve greater sensor durability, strategies to increase the efficiency of toehold strand displacement (86) and improve the robustness (87) of gold-bound thiolated sensors to desorption could be applied.

PDGF-BB Detection. To further demonstrate the modularity of the lily pad sensor and to test its capability for detecting larger analytes, DNA adapter strands were designed to display an aptamer that binds platelet-derived growth factor homodimer of subunit B (PDGF-BB) (Fig. 6). Since the design of the sensor requires two binding events, one to the origami and one to the surface, PDGF-BB was chosen as the analyte due to its homodimeric nature, which allows for the same aptamer to be used on both the origami and the surface. Surface preparation and origami folding were performed as for previous designs, and adapter strands were added after origami had been tethered to the surface, as with the streptavidin sensor. The two adapters (Fig. 6*A*) were designed to have sequences x' and y', followed by a previously reported 36 nt aptamer with an apparent binding affinity to PDGF-BB of 36 fM (88). The resulting sensor achieved detection of PDGF-BB at concentrations as low as 500 pM (Fig. 6*B*), with a signal change of 20%. Sensor signals were stable after PDGF-BB addition for over 100 min of serial monitoring every 5 min, highlighting the functional stability of lily pad sensors. The lowest concentration measured is within one order of magnitude of the best sensitivity

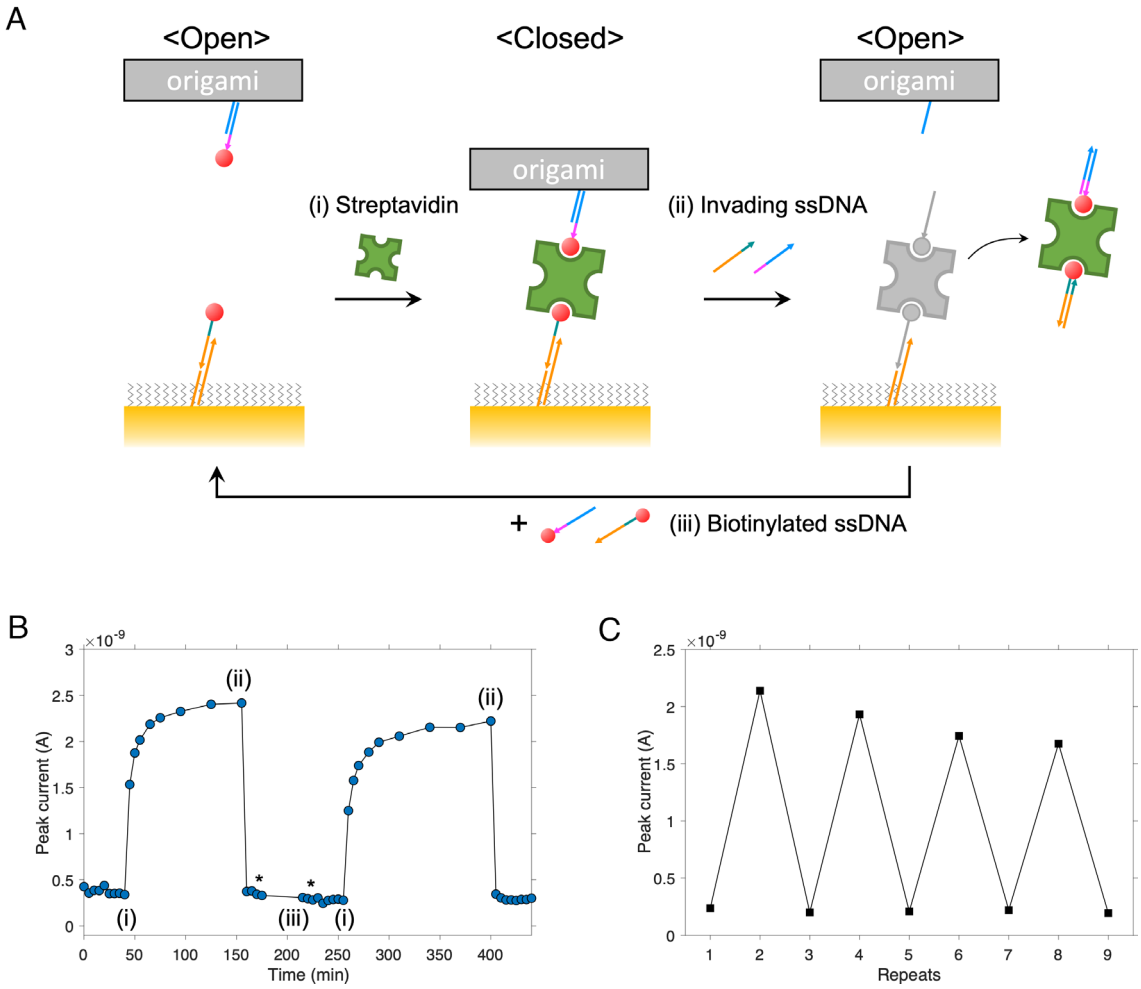

Fig. 5. Lily pad sensors with tightly bound analytes can be regenerated multiple times. (*A*) Schematic shows a lily pad being closed by streptavidin (i), reopened by ssDNA invaders via strand displacement (ii), and regenerated by the addition of new biotin-modified adaptors (iii). (*B*) Sensorgram demonstrating two rounds of streptavidin detection where notations are made for buffer washes (*) and the addition of 500 pM streptavidin (i), 100 nM invaders (ii), and 500 pM biotinylated adaptor strands. (*C*) Changes to SWV signal through four rounds of lily pad regeneration. In each round, streptavidin solution (10 μL, 500 pM) was reacted for 1 h at 34 °C before a measurement was taken (high values). Lily pads with 40 bp MB reporters and *L* = 34 bp were used for (*B*) and (*C*).

achieved for previously reported aptamer-based PDGF-BB sensors (89). However, we note that because the goal of these experiments was simply to demonstrate platform modularity, no efforts were made to co-optimize the aptamer and sensor (e.g., matching aptamer size and MB curtain length); there is therefore, potential to improve the sensitivity of the PDGF-BB version of the lily pad sensor in future work.

Discussion and Conclusion

Using DNA origami, we designed and fabricated a nanodevice—the lily pad—and developed it to create a single-step, reagentless biosensor platform whose modularity enables it to detect arbitrary DNA sequences and proteins through electrochemical measurements. We showed that the modularity of our DNA origami sensor allows the sensing of analytes of varied size and binding properties via simple addition of a few unmodified oligo strands to the base sensor system. The conformational change required for signal is built into the architecture of our sensor, obviating the need to find or engineer binders that undergo a conformational change. Thus, the versatility of our sensing platform should only be limited by the ability to functionalize the binding sites of the lily pad. The lily pad can be trivially modified to use the large variety of available aptamers (90, 91). Conjugating oligos to other binder classes such as antibodies, antibody fragments (92), nanobodies (54), or peptides (93) will allow for their facile incorporation into the lily pad. Whenever it is difficult or simply too expensive to get two binders from the same class, hybrid sensors mixing binders from two classes, e.g., antibodies and aptamers (94), could be used. Larger binders and/or larger analytes may be accommodated by longer MB curtains or redesign of the lily pad geometry to provide a pocket for the analyte–binder stack.

In all versions presented here, the lily pad sensors use two binders. In this sensing modality, lily pads can be customized to detect any analytes which are either multimers (for which both the origami and the electrode present the same binder), or have two distinct epitopes (for which the origami and electrode present distinct binders). To access the sensing of analytes with only one available epitope (e.g., small molecules and some proteins), an appropriate split aptamer (95) or aptamer switch (42, 96) could be incorporated into the lily pad. In the case of a split aptamer modality, one-half of the aptamer would be attached to the origami, and the other half would be attached to the electrode. Analyte binding to both halves would create a bridge and close the lily pad. In the case of an aptamer switch modality, an aptamer re-engineered to have an "antisense" domain (39) partially complementary to the analyte-binding region of the aptamer would be attached to the origami. A sequence complementary to the antisense domain would be attached to the electrode. Upon analyte binding of the aptamer, the antisense domain would be

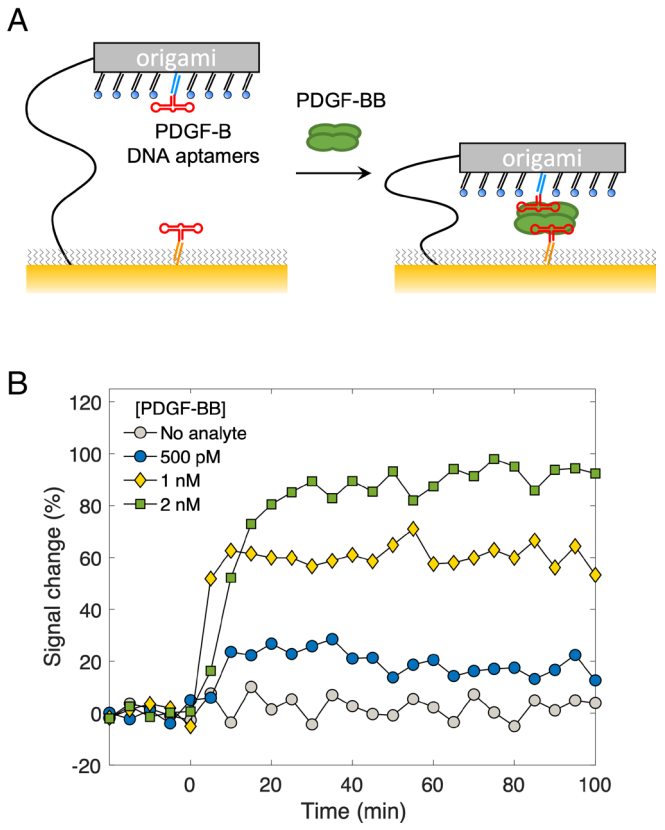

Fig. 6. Lily pad sensors can be adapted to detect a clinically relevant protein biomarker. (*A*) We functionalized lily pad sensors with PDGF binding aptamers. The length and sequence of *x* and *y* adapters were identical to those used in Fig. 3*C*, as was the sensor preparation and interrogation protocol. (*B*) Here we show the continuous interrogation of the lily pad PDGF sensor before and after independent addition of three protein concentrations at $t = 0$ min. The rms of the baseline (i.e., no PDGF) is ±7%. Relative to this baseline, the signal to noise ratio (SNR) for each protein challenge is $SNR_{0.5nM} = 2.8$, $SNR_{1nM} = 8.5$, and $SNR_{2nM} = 13$. Lily pad sensors were interrogated every 4 min via SWV, using parameters indicated in *SI Appendix*.

displaced and bind to its surface complement, thus closing the lily pad. Capture SELEX (41, 42) naturally generates switching aptamers with an appropriate antisense domain, and would obviate the need for aptamer re-engineering. Overall, however, split aptamer and aptamer switch modalities would add significant complexity, and can have a poor success rate for some targets (42); thus we expect that aside from the case of small molecules, a sandwich modality will be the preferred format for lily pad sensors.

The modularity of the lily pad provides benefits beyond simply altering the sensor's target specificity: e.g., we used a library of swappable linkers and curtain strands to optimize sensor performance. Through this approach, we obtained ssDNA (Fig. 2) and streptavidin sensors (Figs. 3 and 4) that can translate picomolar-range changes in analyte concentration to many-fold changes in signal, achieving gains that significantly surpass existing E-DNA/E-AB sensors. The same library could be used to optimize gain and LoD of lily pad sensors that use any of the binders or sensing modalities (sandwich, split aptamer, or aptamer switch) described above.

Beyond sensor optimization, modularity enables practical chip and sensor reuse. When testing different lily pad designs, we reused chips over ten times by simply treating them with hot water to remove one sensor from the surface linkers, and then adding a new sensor. In separate experiments, our streptavidin sensor regeneration method showed that sensors themselves could be reset to unbound state even with a tightly bound ligand such as streptavidin, simply by using toehold-mediated strand displacement, and rebinding fresh biotin-displaying adaptor strands. Furthermore, this approach suggests that sensor specificity could be completely changed "on the fly," by exchanging the analyte binding domain using different binder displaying adaptor strands at every cycle of regeneration, using only these mild, nondenaturing strand displacement reactions.

Similar to E-AB sensors, our platform is reagentless and signaling relies on target-binding induced conformational change—it thus has the potential to work in complex biological matrices, in vivo and ultimately in awake behaving animals. Achieving this potential will require strategies to increase the lifespan of the electrode and monolayer in serum (97). Hardening origami to nuclease degradation, low Mg^{2+} concentrations, and nonspecific binding in vivo, while maintaining its structure and functionality, would also be necessary. Such hardening has been achieved by a variety of methods (98) including increasing helical packing density, chemical cross-linking, coating with block copolymers and functionalization with unnatural nucleotides and end-groups; these methods should translate readily to the lily pad.

Finally, the lily pad design is not limited to electrochemical readout; any readout modality for which signal can be generated by a conformational change should work. With potential modification to the reporter molecules, energy-transfer based fluorescence, surface plasmon resonance, biolayer interferometry, and field effect techniques would all serve as effective readouts for the molecular architecture we describe.

Materials and Methods

dsDNA Linker Preparation. For synthesis of double-stranded DNA linkers with defined length and single-stranded overhangs with specific sequences, we performed two sequential PCRs, extension and autosticky PCRs (99), using Lambda DNA purchased from Promega (WI) and Taq polymerase from New England Biolabs (MA). In the extension PCR, each of the DNA primers (sequences in *SI Appendix*, Table S2), purchased from IDT (CA), consists of a 20 nt long template-binding region that determines the length of the linker and another 20 nt long extension region that determines the terminal sequences of the amplicon added to the sequence from the template DNA (*SI Appendix*, Fig. S2, *Top*). The amplicons from the first PCR, after purification by agarose gel extraction using Zymoclean Gel DNA Recovery Kits purchased from Zymo Research (CA), were used in the second autosticky PCR as template DNA. Each of the primers used in the autosticky PCR (*SI Appendix*, Fig. S2, *Bottom*) contains two domains separated by an abasic site, a 20 nt long template-binding region, identical to the extended sequence in the first PCR, and an overhang sequence chosen for binding to either the flat DNA origami or gold surface. The PCR products were purified using the DNA Clean and Concentrator Kit from Zymo Research and stored in 10 mM Tris buffer (pH 7.4) at −20 °C.

DNA Origami Design and Folding. The DNA origami we used to prepare the lily pads is derived from a structure used in earlier work (49), which was designed in caDNAno (100) to be a flat, circular shape with a square opening. In that work the square opening gave the design a specific orientation on a microfabricated surface; here the square opening is irrelevant. For the purposes of this work, the design was modified so that extensions of staples on the 5′ end would all appear on the same side (*SI Appendix*, Fig. S8). Most staple strands (see *SI Appendix*, Table S5 for sequences) were ordered from IDT unpurified at 100 μM in water and stored at −20 °C. To introduce an analyte binding site near the center for DNA sensing experiments, one staple strand was replaced by a new DNA oligo (IDT, PAGE-purified) that has a 14 nt long 5′ extension (shown in cyan in *SI Appendix*, Fig. S8). To create 20 bp MB curtains: 1) 70 out of 234 total staples were extended on their 5′ ends with a common 20-nt-long single-stranded linker and 2) an MB-modified DNA strand (IDT, dual-HPLC purified) with a sequence complementary to the 20 nt linker was hybridized to all 70 extended staples.

When preparing the lily pads with longer MB curtain lengths (40 or 60 bp) for streptavidin sensing experiments, slightly different schemes were used, as shown at *Right* in Fig. 3*B*. For 40 bp curtains: 1) a 40 nt MB-modified strand (IDT, Dual-HPLC purified) was hybridized to the standard 20 nt extension, and 2) a single 20

nt "cap" ssDNA strand was hybridized to the 3′ end of the MB-modified strand to create a fully duplexed curtain. For 60 bp curtains, origami were functionalized with 40 nt extensions that hybridized the 40 nt MB-modified strand via the same 20 nt overlap used for 40 bp curtains. This meant that to create a fully duplexed curtain, both the 20 nt cap described above, a second 20 nt cap were used (where the second cap was hybridized to the section of the staple extension that was proximal to the origami.)

To synthesize origami, we mixed 8,094 nt long scaffold strands (p8094 from Tilibit, Germany), with the staple strand mixture, MB modified DNA oligos (IDT), and the dsDNA linker from PCRs to the final concentrations given in *SI Appendix*, Table S4 (1:1 scaffold:linker, 5 nM each). One staple on the left side of the origami (yellow orange in *SI Appendix*, Fig. S8) was omitted to leave a position on the scaffold at which the dsDNA linker overhang could bind. Throughout this work, we refer to 1× TAE buffer (Biorad, pH 7.5) with 12.5 mM $MgCl_2$ as "TAE/Mg." 100 μL of scaffold/staple/linker mixture in TAE/Mg was heated to 90 °C for 5 min and annealed from 90 °C to 20 °C at −1°C/min. The final concentration of origami, based on the initial scaffold concentration was 5 nM and the solution was then diluted for use to 2 nM in TAE/Mg buffer.

Lily Pads Assembly on Gold Surface. We use the template-stripping (TS) method to prepare ultraflat (see AFM, *SI Appendix*, Fig. S4) gold surfaces as a substrate for lily pad sensors (58). First, a 200 nm gold film was deposited on a 4 inch silicon wafer (University Wafers, MA) using a Labline electron beam evaporator (Kurt J. Lesker Company, PA) at the Kavli Nanoscience Institute Lab at Caltech. The wafer was then cut to 5 × 8 mm^2 chips by Dynatex GST-150 Scriber/Breaker. A 10 × 10 mm^2 glass coverslip (#2) was rinsed with acetone, isopropyl alcohol, and water, blown dry with nitrogen, and cleaned by oxygen plasma for 5 min in a PE-50 plasma system (Plasma Etch, NV). About 1 μL of UV-curable adhesive (Noland, No.61) was applied on a clean glass and a gold chip was placed on top of the adhesive. The adhesive was then cured via a long-wave UV irradiation for 1 h (66). Right before use, the silicon wafer was pried off the gold/adhesive/glass layers using a razor blade, exposing the ultraflat gold surface on a glass coverslip. To create a well and isolate the reactive area, a silicone gasket (Grace Bio-Labs Press-To Seal silicone isolator, 2 mm diameter) was glued on top and copper tape was used to form an electrical connection.

Two thiolated DNA oligos were purchased from IDT, one for analyte binding (5′-HS-TTTTTAGCTTTGATATCTG3′) and the other for origami–linker tethering on gold (5′CGTAAACCCAGCGTCTTCACCACGATGAATACTCCCACCGTTTTT-SH-3′). In separate tubes, we mixed 1 μL of 100 μM thiolated DNA oligos and 1 μL of 10 mM tris(2-carboxyethyl) phosphine hydrochloride (TCEP, Sigma Aldrich) and incubated for 1 h at room temperature to reduce the disulfide bonds. Then the solutions were mixed and diluted to 100 nM of each DNA in 1× PBS buffer (pH 7.4). 20 μL of the solution was introduced into a silicone gasket well on a freshly prepared TS-gold chip and a Teflon cell (CH instrument, TX) was assembled creating about 1.5 mL of reaction volume that allows three electrode connections. After 1 h incubation at room temperature, the solution was exchanged with 50 μL of 10 mM 6-mercapto-1-hexanol (6-MCH, Sigma Aldrich) in 1× PBS buffer followed by overnight incubation at room temperature for formation of a passivating layer on the gold surface. After this step, the surface presumably had a random distribution of analyte binding and origami linker strands in a 1:1 ratio, with the spaces between these oligos filled by 6-MCH. The density of oligos on these chip surfaces was determined by binding a complementary methylene blue functionalized strand to the chip, and determining total methylene blue occupancy by cyclic voltammetry (*SI Appendix*, Fig. S5).

When annealing the lily pad origami structure, we optimized the concentration of the dsDNA linker so that most of the linker was attached to the origami (*SI Appendix*, Fig. S3). In downstream steps, this allowed us to treat the amount of free linkers as negligible and use the annealed origami mixture without purification. After the passivation step, the 6-MCH solution was removed and 20 μL of 2 nM MB-modified lily pad solution was added in the reaction well of the silicone gasket and incubated for 30 min at room temperature for origami–linker placement on gold via 40 bp DNA hybridization. Then the gold surface was thoroughly rinsed with TAE/Mg to remove the unbound DNA origami, staple strands, and MB-modified DNA oligos.

Chips were reused (often more than 10 times) by detaching the lily pads and analytes from the surface through rinsing with hot water (65° C), by pipetting it directly onto the cell in 100 μL steps for a total of 15 to 20 times. We confirmed zero MB signal via SWV and cyclic voltammetry measurements after water rinsing.

Electrochemical Measurements. A Metrohm PGSTAT 128 N (Netherlands) potentiostat was used for SWV (*SI Appendix*, Fig. S6). After equilibrating the cell at −0.15 V, SWV measurements were performed at a frequency of 10 Hz (see *SI Appendix*, Fig. S7 for optimization) with an amplitude of 25 mV between −0.15 V and −0.4 V relative to Ag/AgCl reference electrode in 1 mL of TAE/Mg at 34 °C; temperature was controlled by using a Coy Labs glove box–without strict temperature control sensor response was too variable. SWV voltammograms were recorded every 5 min for 1 h before and 5 h after the addition of analyte DNA, if not otherwise specified. The first hour of measurements before adding analyte is used to set the baseline, off-signal, and measure the fold-increase. To determine the peak current value a linear baseline is subtracted from the measurement and the MB peak is isolated. This peak is then fit to a Gaussian (101) and its maximum value is recorded as the peak current (*SI Appendix*, Fig. S6 and Text S8).

Streptavidin Detection. Two biotin-modified strands were ordered from IDT, one to create a surface binding site, complementary to the DNA analyte binding thiolated strand (5′-BiotinCAGATATCAAAGCT-3′), and the other to create a binding site on origami, complementary to the DNA analyte binding tail (5′CTGAATGGTACGGA-Biotin-3′). The DNA sensing chip was incubated for 30 min with 500 pM of each of these two strands in TAE/Mg at room temperature. This resulted in an $L = 14$ sensor. After rinsing with TAE/Mg, SWV measurements were performed for 500 pM streptavidin (Thermo Fischer Scientific) at 34 °C in the same buffer.

To create streptavidin sensors with dsDNA surface linkers having a length greater than 14 bp (Fig. 3*C*), we immobilized one of three different 3′-thiolated ssDNAs (10, 20, or 30 nt long) instead of the standard 5′-thiolated sequence; we then performed a 6-MCH passivation step. Next, a 30 min incubation was performed to simultaneously hybridize the lily pads to the surface, and add bridging strands where necessary. In particular, 5 μM of 24, 34, or 44 nt ssDNA bridging strands were added. The 5′ sequence of these strands was complementary to one of the 10, 20, or 30 nt ssDNA already on the surface (as appropriate), so they formed dsDNA complexes proximal to the surface; the 14 nt 3′ end of these strands projected ssDNA tails having the sequence *y*′ into solution. In the next step where the biotin adapter strands (500 pM) were added, one of the adapters bound to the *y*′ tails extending from the surface, forming dsDNA linkers with $L = 24$, 34, or 44 bp.

For LoD experiments in Fig. 4, after rinsing off excess biotin adaptor strands, we measured SWV signal five times before and five times after incubation with the relevant streptavidin solution on the chip; the pre- and postbinding signal for each chip was calculated as the mean of these values. Between the measurements, 10 μL of varying concentrations of streptavidin samples were introduced into a gasket well on the chip, and sealed with a piece of Parafilm to prevent sample evaporation. After 1 h incubation at 34 °C, chips were thoroughly washed with TAE/Mg buffer before the endpoint measurements. This process was repeated for 5 different chips per streptavidin concentration.

For regeneration experiments in Fig. 5, two 19 nt biotinylated adapters (binding region + 5 nt toehold) were used, instead of our standard 14 nt ones. After a streptavidin measurement was finished, the chip was regenerated by adding 100 nM of 19 nt DNA strands that are fully complementary to the adapters, which displace them from the origami and surface sites, returning the chip to the DNA sensing configuration. To finish regeneration of the streptavidin sensor, the chip was incubated with new biotin-modified adapter strands (500 pM, room temperature, 30 min).

PDGF-BB Detection. To create PDGF-BB detecting lily pad sensors, DNA aptamers for PDGF-BB protein (5′CAGGCTACGGCACGTAGAGCATCACCATGATCCTG-3′) were ordered from IDT with two 14 nt extensions, one at 3′-end for binding to the thiolated DNA strands immobilized on gold surface (5′-CAGATATCAAAGCT-3′) and the other at 5′-end for the single-stranded DNA tail on origami (5′-CTGAATGGTACGGA-3′) that were used for the DNA analyte and streptavidin detection studies (*SI Appendix*, Table S3). PDGF-BB protein was ordered from PeproTech, Inc. (NJ). After preparing a standard DNA analyte detecting lily pad sensor, the chip was incubated with 1 nM each of the PDGF-BB aptamers with extensions in TAE/Mg at room temperature. The chip, assembled in a Teflon cell,

was rinsed in the same buffer and connected to potentiostat. SWV measurements were performed as described above in 1 mL of TAE/Mg at 30 °C. After recording SWV voltammograms every 5 min for 1 h, 0, 500 pM, 1 nM, or 2 nM of PDGF-BB protein in the same buffer was added.

Data, Materials, and Software Availability. All study data are included in the article and/or *SI Appendix*.

ACKNOWLEDGMENTS. P.S.L. is grateful for support from Army Research Office (awards W911NF-19-1-0326 and W911NF-231-0283). P.W.K.R. acknowledges support from the Office of Naval Research (awards N00014-18-1-2649 and DURIP N00014-19-1-2341) which provided P.W.K.R, B.J., M.M.G., and J.M.S. with partial support. M.M.G. acknowledge NSF Award No. 2134772 for partial support. J.M.S. acknowledges a fellowship from the Life Sciences Research Foundation supported by Merck Research Laboratories. We thank the Kavli Nanoscience Institute Lab at Caltech for access to fabrication equipment.

Author affiliations: [a]Department of Bioengineering, California Institute of Technology, Pasadena, CA 91125; [b]Department of Bioengineering, University of California, Los Angeles, CA 90095; [c]Department of Mechanical Engineering, Massachusetts Institute of Technology, Cambridge, MA 02139; [d]Department of Pharmacology and Molecular Sciences, Johns Hopkins University School of Medicine, Baltimore, MD 21205; [e]Département de chimie, Université de Sherbrooke, Sherbrooke, QC J1K 2R1, Canada; [f]Department of Chemistry and Biochemistry, University of California Santa Barbara, Santa Barbara, CA 93106; and [g]Department of Chemistry, St. John's University, New York, NY 11439

Author contributions: B.J., M.M.G., J.M.S., A.G., N.A.-C., P.D.-D., K.W.P., P.S.L., and P.W.K.R. designed research; B.J., M.M.G., J.M.S., and E.W. performed research; B.J. contributed new reagents/analytic tools; B.J., M.M.G., and P.W.K.R. analyzed data; and B.J., M.M.G., J.M.S., E.W., A.G., N.A.-C., P.D.-D., K.W.P., P.S.L., and P.W.K.R. wrote the paper.

1. M. R. Jones, N. C. Seeman, C. A. Mirkin, Programmable materials and the nature of the DNA bond. *Science* **347**, 1260901 (2015).
2. N. C. Seeman, H. F. Sleiman, DNA nanotechnology. *Nat. Rev. Mater.* **3**, 17068 (2017).
3. A. Idili *et al.*, A programmable electrochemical Y-shaped DNA scaffold sensor for the single-step detection of antibodies and proteins in untreated biological fluids. *Adv. Funct. Mater.* **32**, 2201881 (2022).
4. H. Pei *et al.*, Regenerable electrochemical immunological sensing at DNA nanostructure decorated gold surfaces. *Chem. Commun.* **47**, 6254 (2011).
5. C. Li *et al.*, Design of DNA nanostructure-based interfacial probes for the electrochemical detection of nucleic acids directly in whole blood. *Chem. Sci.* **9**, 979–984 (2017).
6. J. Xuan, Z. Wang, M. Xiao, H. Pei, Engineering of Interfaces with tetrahedra DNA nanostructures for biosensing applications. *Anal. Sens.* **3**, e202200100 (2022).
7. P. W. K. Rothemund, Folding DNA to create nanoscale shapes and patterns. *Nature* **440**, 297–302 (2006).
8. S. M. Douglas *et al.*, Self-assembly of DNA into nanoscale three-dimensional shapes. *Nature* **459**, 414–418 (2009).
9. S. Wang *et al.*, DNA origami-enabled biosensors. *Sensors* **20**, 6899 (2020).
10. L. Shen, P. Wang, Y. Ke, DNA nanotechnology-based biosensors and therapeutics. *Adv. Heal. Mater.* **10**, 2002205 (2021).
11. P. Pitikultham *et al.*, Stimuli-responsive DNA origami nanodevices and their biological applications. *ChemMedChem* **17**, e202100635 (2022).
12. A. Kuzuya, Y. Sakai, T. Yamazaki, Y. Xu, M. Komiyama, Nanomechanical DNA origami 'single-molecule beacons' directly imaged by atomic force microscopy. *Nat. Commun.* **2**, 449 (2011).
13. A. Kuzuya *et al.*, Nanomechanical DNA origami pH sensors. *Sensors* **14**, 19329–19335 (2014).
14. M. Endo *et al.*, Single-molecule visualization of the activity of a Zn^{2+}-dependent DNAzyme. *Angew. Chem. Int. Ed. Engl.* **54**, 10550–10554 (2015).
15. D. Koirala *et al.*, Single-molecule mechanochemical sensing using DNA origami nanostructures. *Angew. Chem. Int. Ed. Engl.* **53**, 8137–8141 (2014).
16. M. W. Hudoba, Y. Luo, A. Zacharias, M. G. Poirier, C. E. Castro, Dynamic DNA origami device for measuring compressive depletion forces. *ACS Nano* **11**, 6566–6573 (2017).
17. M. Schickinger, M. Zacharias, H. Dietz, Tethered multifluorophore motion reveals equilibrium transition kinetics of single DNA double helices. *Proc. Natl. Acad. Sci. U.S.A.* **115**, E7512–E7521 (2018).
18. P. Shrestha *et al.*, Single-molecule mechanical fingerprinting with DNA nanoswitch calipers. *Nat. Nanotechnol.* **16**, 1362–1370 (2021).
19. C. H. Hansen, D. Yang, M. A. Koussa, W. P. Wong, Nanoswitch-linked immunosorbent assay (NLISA) for fast, sensitive, and specific protein detection. *Proc. Natl. Acad. Sci. U.S.A.* **114**, 10367–10372 (2017).
20. A. R. Chandrasekaran *et al.*, DNA nanoswitch barcodes for multiplexed biomarker profiling. *Nano Lett.* **21**, 469–475 (2021).
21. E. S. Andersen *et al.*, Self-assembly of a nanoscale DNA box with a controllable lid. *Nature* **459**, 73–76 (2009).
22. M. S. Tang *et al.*, An aptamer-enabled DNA nanobox for protein sensing. *Nanomed. Nanotechnol.* **14**, 1161–1168 (2018).
23. D. Selnihhin, S. M. Sparvath, S. Preus, V. Birkedal, E. S. Andersen, Multifluorophore DNA origami beacon as a biosensing platform. *ACS Nano* **12**, 5699–5708 (2018).
24. A. Kuzyk *et al.*, Reconfigurable 3D plasmonic metamolecules. *Nat. Mater.* **13**, 862–866 (2014).
25. T. Funck, F. Nicoli, A. Kuzyk, T. Liedl, Sensing picomolar concentrations of RNA using switchable plasmonic chirality. *Angew. Chem. Int. Ed. Engl.* **57**, 13495–13498 (2018).
26. C. Zhou, L. Xin, X. Duan, M. J. Urban, N. Liu, Dynamic plasmonic system that responds to thermal and aptamer-target regulations. *Nano Lett.* **18**, 7395–7399 (2018).
27. Y. Huang, M. K. Nguyen, A. K. Natarajan, V. H. Nguyen, A. Kuzyk, A DNA origami-based chiral plasmonic sensing device. *ACS Appl. Mater. Inter.* **10**, 44221–44225 (2018).
28. N. Arroyo-Currás, P. Dauphin-Ducharme, K. Scida, J. L. Chávez, From the beaker to the body: Translational challenges for electrochemical, aptamer-based sensors. *Anal. Methods* **12**, 1288–1310 (2020).
29. A. Scott *et al.*, A smartphone operated electrochemical reader and actuator that streamlines the operation of electrochemical biosensors. *ECS Sens. Plus* **1**, 014601 (2022).
30. N. Arroyo-Currás, P. A. V. Jacob Somerson, K. L. Ploense, T. E. Kippin, K. W. Plaxco, Realtime measurement of small molecules directly in awake, ambulatory animals. *Proc. Natl. Acad. Sci. U.S.A.* **114**, 645–650 (2017).
31. J. Gerson *et al.*, High-precision monitoring of and feedback control over drug concentrations in the brains of freely moving rats. *Sci. Adv.* **9**, eadg3254 (2023).
32. C. Fan, K. W. Plaxco, A. J. Heeger, Electrochemical interrogation of conformational changes as a reagentless method for the sequence-specific detection of DNA. *Proc. Natl. Acad. Sci. U.S.A.* **100**, 9134–9137 (2003).
33. Y. Xiao, A. A. Lubin, B. R. Baker, K. W. Plaxco, A. J. Heeger, Single-step electronic detection of femtomolar DNA by target-induced strand displacement in an electrode-bound duplex. *Proc. Natl. Acad. Sci. U.S.A.* **103**, 16677–16680 (2006).
34. T. J. Zwang, E. C. M. Tse, J. K. Barton, Sensing DNA through DNA charge transport. *ACS Chem. Biol.* **13**, 1799–1809 (2018).
35. Y. Xiao, A. A. Lubin, A. J. Heeger, K. W. Plaxco, Label-free electronic detection of thrombin in blood serum by using an aptamer-based sensor. *Angew. Chem. Int. Ed. Engl.* **44**, 5456–5459 (2005).
36. J. Hu, T. Wang, J. Kim, C. Shannon, C. J. Easley, Quantitation of femtomolar protein levels via direct readout with the electrochemical proximity assay. *J. Am. Chem. Soc.* **134**, 7066–7072 (2012).
37. M. A. Pellitero, A. Shaver, N. Arroyo-Currás, Critical review–Approaches for the electrochemical interrogation of DNA-based sensors: A critical review. *J. Electrochem. Soc.* **167**, 037529 (2019).
38. Y. Xiao, T. Uzawa, R. J. White, D. DeMartini, K. W. Plaxco, On the signaling of electrochemical aptamer-based sensors: Collision- and folding-based mechanisms. *Electroanalysis* **21**, 1267–1271 (2009).
39. R. J. White, A. A. Rowe, K. W. Plaxco, Re-engineering aptamers to support reagentless, self-reporting electrochemical sensors. *Analyst* **135**, 589–594 (2010).
40. Y. Wu *et al.*, Using spectroscopy to guide the adaptation of aptamers into electrochemical aptamer-based sensors. *Bioconjugate Chem.* **34**, 124–132 (2023).
41. R. Stoltenburg, N. Nikolaus, B. Strehlitz, Capture-SELEX: Selection of DNA aptamers for aminoglycoside antibiotics. *J. Anal. Methods Chem.* **2012**, 415697 (2012).
42. K. A. Yang, R. Pei, M. N. Stojanovic, In vitro selection and amplification protocols for isolation of aptameric sensors for small molecules. *Methods* **106**, 58–65 (2016).
43. S. Han, W. Liu, S. Yang, R. Wang, Facile and label-free electrochemical biosensors for microRNA detection based on DNA origami nanostructures. *ACS Omega* **4**, 11025–11031 (2019).
44. P. Williamson, H. Ijäs, B. Shen, D. K. Corrigan, V. Linko, Probing the conformational states of a pH-sensitive DNA origami zipper via label-free electrochemical methods. *Langmuir* **37**, 7801–7809 (2021).
45. Z. Ge *et al.*, Constructing submonolayer DNA origami scaffold on gold electrode for wiring of redox enzymatic cascade pathways. *ACS Appl. Mater. Inter.* **11**, 13881–13887 (2019).
46. P. Williamson *et al.*, Signal amplification in electrochemical DNA biosensors using target capturing DNA origami tiles. *ACS Sens.* **8**, 1471–1480 (2023), 10.1021/acssensors.2c02469.
47. E. Pensa, Y. Bogawat, F. C. Simmel, I. Santiago, Single DNA origami detection by nanoimpact electrochemistry. *ChemElectroChem* **9**, e202101696 (2022).
48. N. Arroyo-Currás *et al.*, An electrochemical biosensor exploiting binding-induced changes in electron transfer of electrode-attached DNA origami to detect hundred nanometer-scale targets. *Nanoscale* **12**, 13907–13911 (2020).
49. A. Gopinath *et al.*, Absolute and arbitrary orientation of single-molecule shapes. *Science* **371**, eabd6179 (2021).
50. D. Neupane, K. J. Stine, Electrochemical sandwich assays for biomarkers incorporating aptamers, antibodies and nanomaterials for detection of specific protein biomarkers. *Appl. Sci.* **11**, 7087 (2021).
51. H. Sun *et al.*, Electrochemical sandwich immunoassay for insulin detection based on the use of gold nanoparticle-modified MoS_2 nanosheets and the hybridization chain reaction. *Microchim. Acta* **186**, 6 (2018).
52. R. M. Murphy *et al.*, Size and structure of antigen-antibody complexes. Electron microscopy and light scattering studies. *Biophys. J.* **54**, 45–56 (1988).
53. P. Dauphin-Ducharme *et al.*, Chain dynamics limit electron transfer from electrode-bound, single-stranded oligonucleotides. *J. Phys. Chem. C* **122**, 21441–21448 (2018).
54. M. M. Harmsen, H. J. De Harrd, Properties, production, and applications of camelid single domain antibody fragments. *Appl. Microbiol. Biotechnol.* **77**, 13–22 (2007).
55. J. Hu, T. Wang, J. Kim, C. Shannon, C. J. Easley, Quantitation of femtomolar protein levels via direct readout with the electrochemical proximity assay. *J. Am. Chem. Soc.* **134**, 7066–7072 (2012).
56. N. Arroyo-Curr'as, K. Scida, K. L. Ploense, T. E. Kippin, K. W. Plaxco, High surface area electrodes generated via electrochemical roughening improve the signaling of electrochemical aptamer-based biosensors. *Anal. Chem.* **89**, 12185–12191 (2017).
57. S. Mahshid *et al.*, Mechanistic control of the growth of three-dimensional gold sensors. *J. Phys. Chem. C* **120**, 21123–21132 (2016).
58. M. Hegner, P. Wagner, G. Semenza, Ultralarge atomically flat template-stripped Au surfaces for scanning probe microscopy. *Surf. Sci.* **291**, 39–46 (1993).
59. P. Dauphin-Ducharme, N. Arroyo-Currás, K. W. Plaxco, High-precision electrochemical measurements of the guanine-, mismatch-, and length-dependence of electron transfer from electrode-bound DNA are consistent with a contact-mediated mechanism. *J. Am. Chem. Soc.* **141**, 1304–1311 (2019).
60. H. Ni *et al.*, Direct visualization of floppy two-dimensional DNA origami using cryogenic electron microscopy. *iScience* **25**, 104373 (2022).

61. J. Y. Lee *et al.*, Rapid computational analysis of DNA origami assemblies at near-atomic resolution. *ACS Nano* **15**, 1002–1015 (2021).
62. R. Pandey *et al.*, Integrating programmable DNAzymes with electrical readout for rapid and culture-free bacterial detection using a handheld platform. *Nat. Chem.* **13**, 895–901 (2021).
63. P. Dauphin-Ducharme *et al.*, Simulation-based approach to determining electron transfer rates using square-wave voltammetry. *Langmuir* **33**, 4407–4413 (2017).
64. B. Nordén, F. Tjerneld, Structure of methylene blue–DNA complexes studied by linear and circular dichroism spectroscopy. *Biopolymers* **21**, 1713–1734 (1982).
65. D. F. Bradley, N. C. Stellwagen, C. T. O'konski, C. M. Paulson, Electric birefringence and dichroism of acridine orange and methylene blue complexes with polynucleotides. *Biopolymers* **11**, 645–652 (1972).
66. E. A. Weiss *et al.*, Si/SiO_2-templated formation of ultraflat metal surfaces on glass, polymer, and solder supports: Their use as substrates for self-assembled monolayers. *Appl. Microbiol. Biotechnol.* **77**, 13–22 (2007).
67. A. Shaver, S. D. Curtis, N. Arroyo-Currás, Alkanethiol monolayer end groups affect the long-term operational stability and signaling of electrochemical, aptamer-based sensors in biological fluids. *ACS Appl. Mater. Inter.* **12**, 11214–11223 (2020).
68. S. O. Kelley, J. K. Barton, N. M. Jackson, M. G. Hill, Electrochemistry of methylene blue bound to a DNA-modified electrode. *Bioconjugate Chem.* **8**, 31–37 (1997).
69. N. Borochov, H. Eisenberg, Z. Kam, Dependence of DNA conformation on the concentration of salt. *Biopolymers* **20**, 231–235 (1981).
70. P. J. Hagerman, Flexibility of DNA. *Ann. Rev. Biophys. Biophys. Chern.* **17**, 265–286 (1988).
71. J. Zhang, Y. Huang, N. Trombly, C. Yang, A. Mason, Electrochemical array microsystem with integrated potentiostat. *IEEE Sensors* (2005). https://dx.doi.org/10.1109/ICSENS.2005.1597716. Accessed 25 November 2024.
72. Y. Xiao, B. D. Piorek, K. W. Plaxco, A. J. Heeger, A reagentless signal-on architecture for electronic, aptamer-based sensors via target-induced strand displacement. *J. Am. Chem. Soc.* **127**, 17990–17991 (2005).
73. A. A. Lubin, K. W. Plaxco, Folding-based electrochemical biosensors: The case for responsive nucleic acid architectures. *Accounts Chem. Res.* **43**, 496–505 (2010).
74. R. J. White, K. W. Plaxco, Exploiting binding-induced changes in probe flexibility for the optimization of electrochemical biosensors. *Anal. Chem.* **82**, 73–76 (2010).
75. P. Dauphin-Ducharme, K. W. Plaxco, Maximizing the signal gain of electrochemical-DNA sensors. *Anal. Chem.* **88**, 11654–11662 (2016).
76. C. Davies, "Immunoassay performance measures" in *The Immunoassay Handbook–Theory and Applications of Ligand Binding, ELISA and Related Techniques*, D. Wild, Ed. (Elsevier Science, 2013).
77. M. Sample, M. Matthies, P. Šulc, Hairygami: Analysis of DNA nanostructure's conformational change driven by functionalizable overhangs. *ACS Nano* **43**, 30004–30016 (2024).
78. H. Ni *et al.*, Direct visualization of floppy two-dimensional DNA origami using cryogenic electron microscopy. *iScience* **25**, 104373 (2022).
79. S. Somasundaram, C. J. Easley, A nucleic acid nanostructure built through on-electrode ligation for electrochemical detection of a broad range of analytes. *J. Am. Chem. Soc.* **142**, 11721–11726 (2019).
80. S. Cai *et al.*, Single-molecule amplification-free multiplexed detection of circulating microRNA cancer biomarkers from serum. *Nat. Commun.* **12**, 3515 (2021).
81. K. J. Cash, F. Ricci, K. W. Plaxco, An electrochemical sensor for the detection of protein small molecule interactions directly in serum and other complex matrices. *J. Am. Chem. Soc.* **131**, 6955–6957 (2009).
82. S. S. Mahshid, S. Camiré, F. Ricci, A. Vallée-Bélisle, A highly selective electrochemical DNA-based sensor that employs steric hindrance effects to detect proteins directly in whole blood. *J. Am. Chem. Soc.* **137**, 15596–15599 (2015).
83. S. Somasundaram, C. J. Easley, A nucleic acid nanostructure built through on-electrode ligation for electrochemical detection of a broad range of analytes. *J. Am. Chem. Soc.* **141**, 11721–11726 (2019).
84. A. Idili *et al.*, A programmable electrochemical Y-shaped DNA scaffold sensor for the single-step detection of antibodies and proteins in untreated biological fluids. *Adv. Funct. Mater.* **32**, 2201881 (2022).
85. B. Yurke, A. J. Turberfield, A. P. Mills, F. C. Simmel, J. L. Neumann, A DNA-fuelled molecular machine made of DNA. *Nature* **406**, 605–608 (2000).
86. F. C. Simmel, B. Yurke, H. R. Singh, Principles and applications of nucleic acid strand displacement reactions. *Chem. Rev.* **119**, 6326–6369 (2019).
87. V. Clark, M. A. Pellitero, N. Arroyo-Currás, Explaining the decay of nucleic acid-based sensors under continuous voltammetric interrogation. *Anal. Chem.* **95**, 4974–4983 (2023).
88. C. Q. Vu, P. Rotkrua, Y. Tantirungrotechai, B. Soontornworajit, Oligonucleotide hybridization combined with competitive antibody binding for the truncation of a high-affinity aptamer. *ACS Comb. Sci.* **19**, 609–617 (2017).
89. R. Y. Lai, K. W. Plaxco, A. J. Heeger, Aptamer-based electrochemical detection of picomolar platelet-derived growth factor directly in blood serum. *Anal. Chem.* **79**, 229–233 (2007).
90. A. D. Keefe, S. Pai, A. Ellington, Aptamers as therapeutics. *Nat. Rev. Drug Discov.* **9**, 537–550 (2010).
91. Y. Zhang, B. S. Lai, M. Juhas, Recent advances in aptamer discovery and applications. *Molecules* **24**, 941 (2019).
92. A. L. Nelson, Antibody fragments: Hope and hype. *MAbs* **2**, 77–83 (2010).
93. A. Wada, Development of next-generation peptide binders using in vitro display technologies and their potential applications. *Front. Immunol.* **4**, 224 (2013).
94. M. Jarczewska, E. Malinowska, The application of antibody–aptamer hybrid biosensors in clinical diagnostics and environmental analysis. *Anal. Methods* **12**, 3183–3199 (2020).
95. M. Debiais, A. Lelievre, M. Smietana, S. Müller, Splitting aptamers and nucleic acid enzymes for the development of advanced biosensors. *Nucleic Acids Res.* **48**, 3400–3422 (2020).
96. A. E. Rangel, A. A. Hariri, M. Eisenstein, H. T. Soh, Engineering aptamer switches for multifunctional stimulus-responsive nanosystems. *Adv. Mater.* **32**, 2003704 (2020).
97. Z. Watkins, A. Karajic, T. Young, R. White, J. Heikenfeld, Week-long operation of electrochemical aptamer sensors: New insights into self-assembled monolayer degradation mechanisms and solutions for stability in serum at body temperature. *ACS Sensors* **8**, 1119–1131 (2023).
98. A. R. Chandrasekaran, Nuclease resistance of DNA nanostructures. *Nat. Rev. Chem.* **5**, 225–239 (2021).
99. J. Gál, R. Schnell, S. Szekeres, M. Kálmán, Directional cloning of native PCR products with preformed sticky ends (autosticky PCR). *Mol. Gen. Genet.* **260**, 569–73 (1999).
100. S. M. Douglas *et al.*, Rapid prototyping of 3D DNA-origami shapes with caDNAno. *Nucleic Acids Res.* **37**, 5001–5006 (2009).
101. G. Macfic, J. Atherton, R. Compton, Using microelectrode square-wave voltammetry to monitor the progress of complex homogeneous chemical reactions. *Electroanalysis* **14**, 479–485 (2002).